

# On-Chip Photonic Localization in Aharonov–Bohm Cages Composed of Microring Lattices

Shuyue Chen,<sup>†</sup> Shaolin Ke,<sup>†</sup> Dong Zhao,<sup>†</sup> Jianghua Ye, Yanan Wang, Weiwei Liu,<sup>\*</sup> Kun Huang, Bing Wang,<sup>\*</sup> and Peixiang Lu



Cite This: *Nano Lett.* 2024, 24, 4810–4815



Read Online

ACCESS |

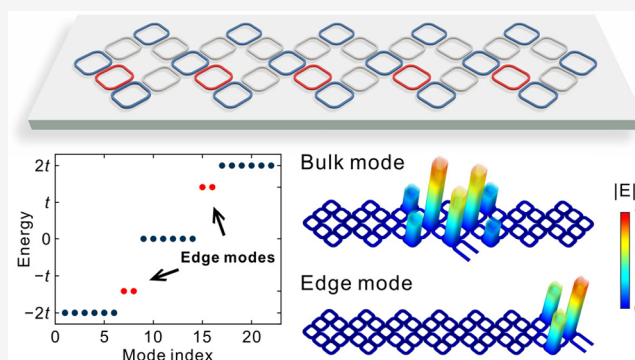
Metrics & More

Article Recommendations

Supporting Information

**ABSTRACT:** Flatband localization endowed with robustness holds great promise for disorder-immune light transport, particularly in the advancement of optical communication and signal processing. However, effectively harnessing these principles for practical applications in nanophotonic devices remains a significant challenge. Herein, we delve into the investigation of on-chip photonic localization in AB cages composed of indirectly coupled microring lattices. By strategically vertically shifting the auxiliary rings, we successfully introduce a magnetic flux of  $\pi$  into the microring lattice, thereby facilitating versatile control over the localization and delocalization of light. Remarkably, the compact edge modes of this structure exhibit intriguing topological properties, rendering them strongly robust against disorders, regardless of the size of the system. Our findings open up new avenues for exploring the interaction between flatbands and topological photonics on integrated platforms.

**KEYWORDS:** *microring resonators, topological photonics, flatband, photonic gauge potential*



avenues for exploring the interaction between flatbands and

Photonic gauge potential introduces a new dimension for light manipulation, paving the way for the design of innovative and compact optical components.<sup>1–4</sup> The artificial photonic gauge potential is an analogy of vector or scalar potential acting on electron wave functions, which can be created through spatial/temporal modulation,<sup>1,5</sup> nonlinear effects,<sup>6</sup> tilted geometry,<sup>7,8</sup> and so on. By appropriately setting position-dependent photonic gauge potentials, a synthetic magnetic field for light can be generated. As a result, a variety of interesting phenomena have been observed, including the photonic Aharonov–Bohm (AB) effect,<sup>2,9</sup> negative refraction,<sup>10</sup> and topologically protected edge modes.<sup>11,12</sup> In particular, the utilization of photonic gauge potential enables to control light delocalization and localization, which is crucial for on-demand modulation of light propagation.<sup>13</sup> One notable example is the AB caging effect in photonic crystals, which produce complete flatbands with constant eigenenergy independent of crystal momentum.<sup>14–19</sup> The underlying mechanism can be attributed to generation of compact localized modes through destructive interference.<sup>20</sup> Compared with regular flat-band systems in which flatbands usually coexist with dispersive ones and only specific excitation is able to induce corresponding localized modes,<sup>21,22</sup> the complete flatbands originated from the AB caging effect are extremely beneficial to excite the localized modes at arbitrary bands in smaller systems.

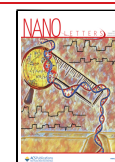
Recently, AB caging effect in optical waveguide systems has garnered significant attention, with the goal of achieving disorder-immune localization.<sup>15,19,23–25</sup> For example, Kremer et al. constructed photonic AB cages using auxiliary waveguides, exhibiting nonquantized Zak’s phase and the robustness of the topological edge modes.<sup>26</sup> In addition, angular-momentum-assisted configurations,<sup>18</sup> topoelectrical circuits<sup>27</sup> and ultracold atoms<sup>28,29</sup> also provided useful platforms for investigating the photonic AB caging effect. In particular, utilization of microring resonators has become one of the favorable approaches for introducing and manipulating the photonic gauge potential. Arbitrary magnetic fluxes can be generated by incorporating auxiliary rings to induce direction-dependent coupling phases.<sup>30</sup> Moreover, the microring systems have extraordinary versatility for precisely engineering parameters including coupling strength, on-site potentials, even with asymmetric couplings.<sup>31–33</sup> Therefore, ideal on-chip platforms have been constructed using the microring resonators to investigate quantum Hall effects,<sup>34</sup> non-

**Received:** December 25, 2023

**Revised:** April 6, 2024

**Accepted:** April 8, 2024

**Published:** April 9, 2024



Hermitian skin effects,<sup>35,36</sup> topological lasers,<sup>37</sup> and anti-PT-symmetric system.<sup>38</sup> Considering the great potential for producing compact localized modes in integrated photonic devices, implementation of AB cages with microring lattices on a chip will hold outstanding promise for the development of functional nanophotonic devices operating at optical communication wavelengths.

In this study, the AB caging effect is investigated and realized in a quasi-one-dimensional (quasi-1D) rhombic chain composed of microring lattices on-chip. Nanophotonic AB cages are designed and implemented by using indirectly coupled microring resonators on a standard silicon-on-insulator (SOI) platform. The microring resonators provide ideal foundations for engineering magnetic fields. Transmission spectra display transmission dips in agreement with theory, validating the excitation of AB caging. By manipulation of photonic gauge potentials, the capability to localize and delocalize light is also demonstrated, thus facilitating the activation or deactivation of the AB caging effect. Moreover, the topological edge modes in the AB cages exhibit remarkable robustness against disorders, regardless of the size of the system.

We start by considering a quasi-1D rhombic lattice comprising indirectly coupled microring resonators, as depicted in Figure 1a. Within each unit cell, there are three lattice sites labeled  $a_n$ ,  $b_n$ , and  $c_n$ . Each plaquette features three positive couplings (denoted as  $t$ ) and one negative coupling ( $-t$ ). Different types of coupling can be engineered between two site rings via link rings, as shown in Figure 1b. These link rings fulfill the condition of antiresonance by introducing an

extra path length  $\Delta L = \pi/(n_{\text{eff}}k_0)$ , where  $n_{\text{eff}}$  and  $k_0$  represent the effective refractive index and wave vector in vacuum, respectively. Such a scheme directly introduces the coupling  $t$  and allows us to arbitrarily manipulate the phase and magnitude of the coupling. By shifting the links with a displacement  $\Delta\eta$ , a spin-dependent phase  $\varphi = n_{\text{eff}}k_0\Delta\eta$  is induced, which is  $\pi$  in our system. As a consequence, both positive and negative couplings can be integrated into each plaquette, resulting in an effective flux of  $\pi$ . The Bloch Hamiltonian of this model in momentum space can be expressed as follows

$$H = t \begin{pmatrix} 0 & 1 + e^{-ik} & -1 + e^{-ik} \\ 1 + e^{ik} & 0 & 0 \\ -1 + e^{ik} & 0 & 0 \end{pmatrix} \quad (1)$$

where  $k$  denotes the Bloch momentum and  $t$  represents the effective coupling strength between adjacent sites. Diagonalizing this matrix yields the corresponding eigenvalues of  $E = -2t, 0$ , and  $2t$ , which remain independent of the momentum  $k$ . The corresponding eigenvectors are given by

$$|v_1\rangle = \frac{1}{2} \begin{pmatrix} 0 \\ -1 + e^{ik} \\ 1 + e^{ik} \end{pmatrix}, |v_2\rangle = \frac{1}{2\sqrt{2}} \begin{pmatrix} -2 \\ 1 + e^{ik} \\ -1 + e^{ik} \end{pmatrix}, |v_3\rangle = \frac{1}{2\sqrt{2}} \begin{pmatrix} 2 \\ 1 + e^{ik} \\ -1 + e^{ik} \end{pmatrix} \quad (2)$$

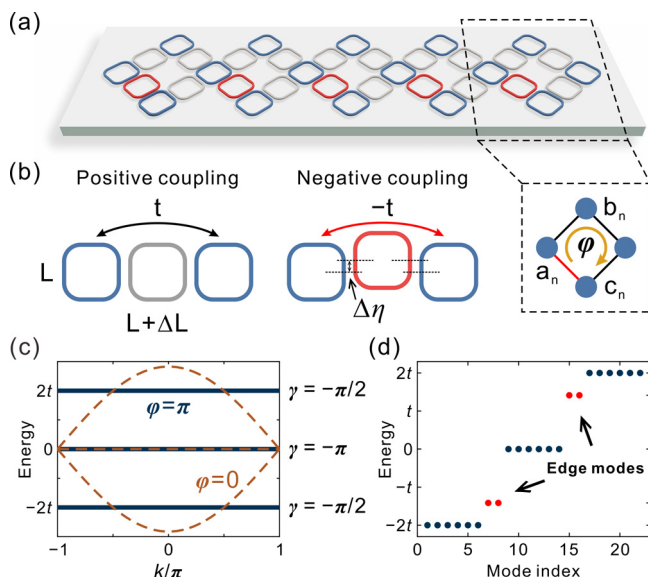


**Figure 1.** Schematic of the Aharonov–Bohm (AB) cages. (a) The geometry of the proposed microring lattice. The unit cell comprises three lattice sites ( $a_n$ ,  $b_n$ , and  $c_n$ ), with each plaquette threaded by a flux  $\varphi$ . (b) Implementation of positive coupling (black arrow) by engineering the link ring (gray). Introducing negative coupling (red arrow) by vertically shifting the link ring. (c) Band structure of the lattice for  $\varphi = 0$  (brown dashed lines) and  $\varphi = \pi$  (blue solid lines) under the periodic boundary condition (PBC). The bands have the Zak's phase of  $\gamma = -\pi/2, -\pi$ , and  $-\pi/2$ , respectively. (d) eigenvalue spectrum under the open boundary condition (OBC). The bulk modes are denoted by blue dots, while the red dots indicate the edge modes.

Figure 1c illustrates energy bands for  $\varphi = 0$  (brown dashed lines) and  $\varphi = \pi$  (blue solid lines) under periodic boundary condition (PBC). Notably, for  $\varphi = 0$ , the system supports a zero-energy flatband coexisting with two dispersive bands. In this scenario, light cannot be localized unless the compact localized eigenstate corresponding to the flatband is excited. In contrast, for  $\varphi = \pi$ , the AB caging effect becomes apparent, in which the flatband system originating from destructive interference allows for light localization in real space with an arbitrary exciting position. On the other hand, the presence of topological edge modes can be predicted using the topological invariant calculated from periodic bulk modes. Here, the topological invariant is determined by the Zak's phase

$$\gamma = i \int_{\text{BZ}} \langle \nu(k) | \partial_k | \nu(k) \rangle dk \quad (3)$$

which is figured out to be  $\gamma = -\pi/2, -\pi$ , and  $-\pi/2$  with top and bottom bands exhibiting nonquantized bulk indices. Nevertheless, the topological origins of this structure can be elucidated by squaring the Hamiltonian matrix, which inherits a nontrivial SSH chain with intra- and intercell couplings of 0 and  $2t^2$ , respectively. Moreover, the system is subject to two nonsymmorphic symmetries, ensuring that they are robust against symmetry-preserved disorders, despite exhibiting non-quantized indices.<sup>26</sup> Consequently, the lattice possesses two topologically nontrivial band gaps, while the topological edge modes arise within the upper and lower band gaps. Figure 1d displays the spectrum of corresponding eigenvalues under open boundary condition (OBC), revealing two in-gap modes at energies  $E = \pm \sqrt{2} t$ . Intriguingly, these emerging edge

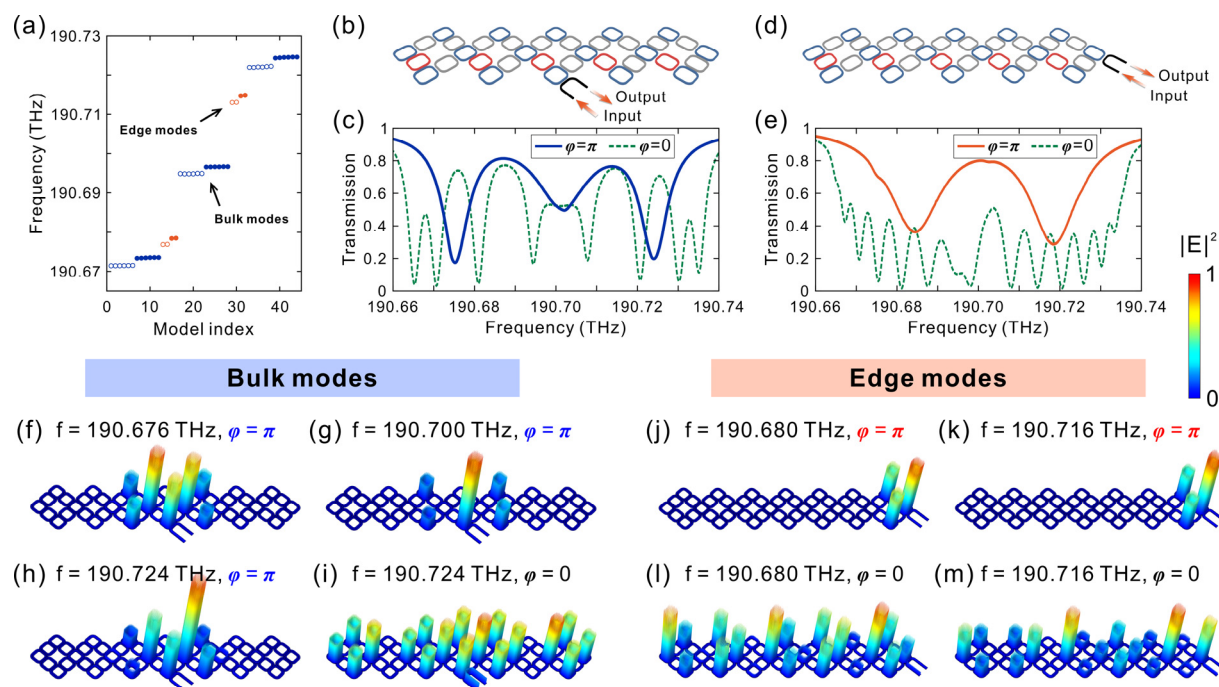


**Figure 2.** Simulated localized modes of excited AB caging effect. (a) Energy spectrum for a finite lattice with  $\varphi = \pi$ . The bulk (edge) modes are indicated by blue (red) dots. (b, d) Schematic of the excitation port locations of the bulk (b) and edge (d) modes, respectively. (c) Transmission spectra for  $\varphi = \pi$  (blue solid line) and  $\varphi = 0$  (green dashed line), corresponding to (b). (e) Transmission spectra for  $\varphi = \pi$  (orange solid line) and  $\varphi = 0$  (green dashed line), corresponding to (d). (f–i) Simulated field distributions ( $|E|^2$ ) of the bulk modes for  $\varphi = \pi$  (at dips transmission frequencies) and  $\varphi = 0$ . (j–m) Simulated field distributions ( $|E|^2$ ) of the edge modes for  $\varphi = \pi$  (at dips transmission frequencies) and  $\varphi = 0$ .

modes also feature completely flat energy bands, exhibiting properties identical with those of the bulk modes.

The dispersion relation in momentum space gives rise to wave localization in a real space. In order to demonstrate the theoretical predictions, light field evolution is simulated, and the corresponding field distributions are examined by using the finite-element method (COMSOL Multiphysics 5.6). Side length of each ring is set to  $10 \mu\text{m}$ , and the four corners are rounded off with a radius of  $3 \mu\text{m}$ . The core width remained fixed at  $0.27 \mu\text{m}$ . The refractive index of the core and cladding materials are  $n_{\text{core}} = 3$  and  $n_{\text{air}} = 1$ , respectively. For the transverse electric (TE) mode, the effective refractive index is calculated to be  $n_{\text{eff}} = 2.465$ . The gaps between rings are set to  $0.375 \mu\text{m}$ . The resonant frequency of the single site ring is determined to be  $f_0 = 190.694 \text{ THz}$ . The simulations maintained a computational grid accuracy of approximately  $50 \text{ nm}$ , ensuring a precise depiction of field distributions upon light excitation. We first simulated the band structure under the OBC. The corresponding simulated spectrum of eigenfrequencies is presented in Figure 2a. It is notable that the spectrum exhibits two distinct sets of eigenvalue distributions (solid and hollow circles), due to the implementation of a synthetic gauge potential that induces pseudospin–orbit interaction, encompassing both clockwise (CW) and counterclockwise (CCW) modes.

First, to excite the bulk modes, the excitation port is located at the center of the system, as illustrated in Figure 2b. Figure 2c plots the calculated transmission spectrum at the output port. For  $\varphi = \pi$  (blue solid lines), narrow dips are readily observed around the incident frequency,  $f = 190.676$ ,  $190.700$ , and  $190.724 \text{ THz}$ , indicating the excitation of bulk modes. These results are in good agreement with those obtained in Figure 2a (blue dots). Furthermore, Figure 2f–h illustrates the

field distributions ( $|E|^2$ ) at the three dips, respectively. As expected, the light is confined near the excitation port, while the link rings remain devoid of light due to antiresonant nature. The compact localization is induced by destructive interference when light is incident into this homogeneous system, rather than localization caused by defects and disorders. For comparison, the transmission spectrum for  $\varphi = 0$  exhibits no regularity (green dashed line). Figure 2i shows the corresponding field distributions ( $|E|^2$ ) at incident frequency  $f = 190.724 \text{ THz}$ . Due to the absence of the gauge flux, the light spreads throughout the entire system without any localization. Therefore, the localization and delocalization of light waves can be manipulated by actively controlling the effective gauge potential  $\varphi$ .

Then, another important aspect regarding the excitation of edge modes is considered. To excite the edge modes, the excitation port is positioned on the right side of the AB cage, as illustrated in Figure 2d. Figure 2e plots the calculated transmission spectrum at the output port. Notably, for  $\varphi = \pi$  (orange solid lines), we observe two distinct and narrow transmission dips at the incident frequency  $f = 190.680$  and  $190.716 \text{ THz}$ . Interestingly, these dips align precisely with the eigenfrequencies of the in-gap states (red dots) shown in Figure 2a. This unequivocally demonstrates the presence of edge states within the lattice. Furthermore, field distributions ( $|E|^2$ ) at these transmission dips are examined, as depicted in Figure 2j and k. Due to destructive interference, the light becomes firmly trapped within a plaquette near the input port, with minimal light propagation into the bulk. In contrast, for  $\varphi = 0$ , it fails to excite the topological edge modes (green dashed line), which can be further confirmed by analyzing the corresponding field distributions (Figure 2l and m). The light is not localized at the edge but rather spreads throughout

the lattice. It is worth noting that there is finite backscattering in the system that makes the CW and CCW modes not degenerate. The mixing of the two pseudospins is equivalent to stacking the lattices and composing a bilayer lattice model with mirror symmetry.<sup>40</sup> The existence of mirror symmetry allows us to divide it into two decoupled subspaces. It is equivalent to shifting the on-site potential of the subsystems without changing the flatbands of the AB cages. Consequently, the mixing will not affect the localization properties of the AB cages.

To realize the AB caging effect on the chip, a quasi-1D rhombic chain composed of microring lattices is designed and fabricated on a standard SOI platform (see Section S1, Supporting Information). Each ring has a cross-section with a width of  $w = 400$  nm and a height of  $h = 220$  nm, specifically tailored to support a single TE-polarized mode at optical communication wavelength of 1550 nm. The edge-to-edge separation between the site ring and link ring is designed to be 150 nm. This gives an effective coupling of 57 GHz (0.91 nm) between site rings, which is obtained by simulating the frequency splitting in a system consisting of two site rings (see Section S2, Supporting Information). As mentioned above, the link rings are designed to be antiresonant with the site rings, which are spatially shifted along the vertical direction to introduce an asymmetric set of hopping phases. The phase shift should follow an integer multiple of  $\Delta\eta = \pi/(n_{\text{eff}}k_0)$ . Herein, the phase shift is designed to be  $\eta = 3\Delta\eta$ , corresponding to a spatial shift of 548 nm. This design minimizes the relative error of the nanofabrication process, sufficiently ensuring a consistent magnetic flux of  $\varphi = \pi$  within each plaquette. Figure 3a displays a top-view SEM image of the fabricated AB caging chain. The periodic rhombic plaquette structure is clearly discernible. Upon closer inspection, the unit cell of the AB caging chain exhibits a regular and smooth surface, as depicted in Figure 3b. Furthermore, the fabricated

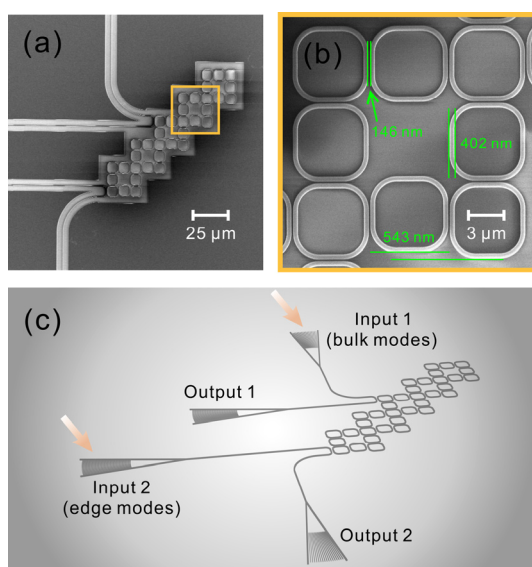


**Figure 3.** Experimental realization of photonic AB cages. (a) Scanning electron microscopy (SEM) image displaying the on-chip AB caging chain. (b) Magnification of the yellow-outlined area indicated in (a), showing a SEM image of a unit cell within the lattice. (c) Schematic diagram of the experimental setup for measuring the AB caging effect. Input port 1 and port 2 are utilized to excite the bulk and edge modes of the lattice, respectively.

nanophotonic structures align well with the intended design, demonstrating the successful realization of the AB cage with microring lattices on the chip.

For optical measurements (see Section S3, Supporting Information), two waveguides connected with grating couplers are strategically positioned in the middle and at the edge of the AB-cage structure to excite bulk and edge modes, respectively, as illustrated in Figure 3c. The transmission spectra of the lattices are measured for each excitation to extract the mode localization properties at the corresponding output ports. Figure 4a displays a transmission spectrum for bulk mode

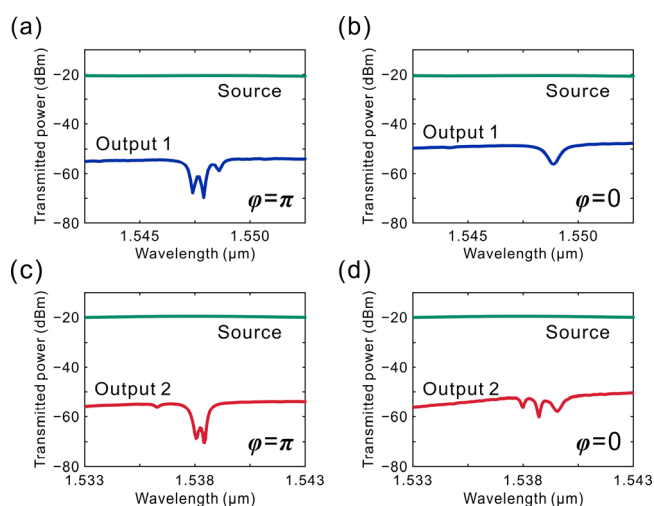


**Figure 4.** Experimentally measured transmission spectra. (a) Transmitted power at output port 1 for  $\varphi = \pi$ , indicating the excitation of the bulk modes. (b) Transmitted power at output port 1 for  $\varphi = 0$ . (c) Transmitted power at output port 2 for  $\varphi = \pi$ , indicating the excitation of the edge modes. (d) Transmitted power at output port 2 for  $\varphi = 0$ . The green lines (source) indicate that light propagates directly from the input to the output without coupling into the lattice.

excitation (port 1), with a gauge potential of  $\varphi = \pi$ . There exist three transmission dips at wavelengths  $\lambda_1 = 1.5474 \mu\text{m}$ ,  $\lambda_2 = 1.5479 \mu\text{m}$ , and  $\lambda_3 = 1.5486 \mu\text{m}$ , respectively, which is consistent with the simulated profiles and indicates the excitation of the localized bulk modes. For comparison, the transmission spectrum of the lattice without photonic gauge potential ( $\varphi = 0$ ) is measured, as shown in Figure 4b. The spectrum displays a broad dip, indicating the lack of specific localized mode. For the edge states, the transmission spectrum of the AB caging structure with  $\varphi = \pi$  is presented in Figure 4c. Two narrow transmission dips can be observed at  $\lambda_1 = 1.5380$  and  $\lambda_2 = 1.5382 \mu\text{m}$ , which correspond to the localized edge modes. In contrast, the lattice without a photonic gauge potential ( $\varphi = 0$ ) is topologically trivial, and no localized properties can be observed, as shown in Figure 4d. It should be noted that experimentally measured spectra for  $\varphi = \pi$  are very consistent with the simulations, indicating that the photonic localization induced by the AB caging effect can still survive even with dissipation in the microring lattices.

What warrants special attention is that the distributions of the topological edge modes in the AB cages do not exhibit the typical exponential decay from the edges, as often observed in

other systems (Figure 2j and 2k). Instead, under the influence of destructive interference, the light remains perfectly confined within one unit cell at the edge. Consequently, we can reasonably anticipate that these edge modes may exhibit remarkable stability and maintain strong topological protection, regardless of the system size.<sup>39</sup> To validate this hypothesis, we discuss the robustness of the topological edge modes in smaller systems. Specifically, we perform numerical calculations to determine the energy offset and localization length of the edge modes and plot them as a function of the disorder strength (see Section S4, Supporting Information). Our findings reveal that the lattice exhibits robust edge modes against general disorders, even independent of the size of the system, which can be attributed to the enhanced topological protection resulting from the AB caging effect. In our measurements, it is observed that the excited bulk modes experience some disorders, leading to imperfect dips in the spectrum (see Figure 4a). This discrepancy can be attributed to imperfections introduced during the nanofabrication, which introduce slight disorder in the resonance frequencies of the rings. Despite the presence of disorders, the stability of the edge modes is preserved, benefiting from the enhanced topological protection of the edge modes in AB cages against on-site detuning terms, even in small systems, as previously elucidated. In addition, the tolerance to fabrication errors of the photonic localization is analyzed (see Section S5, Supporting Information). The localized edge modes remain observable even with a 10% fabrication error, suggesting a great robustness of the photonic AB caging effect against fabrication errors.

In summary, we have undertaken a comprehensive investigation into the photonic AB cages in a rhombic microring lattice. By employing engineered link rings, the lattice achieves a consistent flux of  $\pi$  within each plaquette, thereby enabling the integration of both positive and negative couplings. Subsequently, we analyze the energy bands, explore the topological properties, and demonstrate the localization of both bulk and edge modes. Notably, the phenomenon of localization arises from destructive interference, endowing the AB cages with compact localized edge modes that exhibit exceptional robustness against disorders regardless of the size of the system. Furthermore, through the utilization of a standard SOI platform, experimental measurements conducted on nanofabricated on-chip microring resonators validate the presence of bulk and edge states, effectively showcasing the AB caging effect. These findings underscore the potential of this lattice structure in various applications such as optical communication, signal processing, and the development of compact topological components.

## ■ ASSOCIATED CONTENT

### SI Supporting Information

The Supporting Information is available free of charge at <https://pubs.acs.org/doi/10.1021/acs.nanolett.3c05095>.

Detailed nanofabrication, simulated magnitude of coupling, experimental measurement setup, numerical disorder analysis, and fabrication tolerance analysis (PDF)

## ■ AUTHOR INFORMATION

### Corresponding Authors

**Weiwei Liu** – Wuhan National Laboratory for Optoelectronics and School of Physics, Huazhong University of Science and Technology, Wuhan 430074, China; [orcid.org/0000-0001-9451-1968](https://orcid.org/0000-0001-9451-1968); Email: [lwust@hust.edu.cn](mailto:lwust@hust.edu.cn)

**Bing Wang** – Wuhan National Laboratory for Optoelectronics and School of Physics, Huazhong University of Science and Technology, Wuhan 430074, China; [orcid.org/0000-0002-0180-5623](https://orcid.org/0000-0002-0180-5623); Email: [wangbing@hust.edu.cn](mailto:wangbing@hust.edu.cn)

### Authors

**Shuyue Chen** – Wuhan National Laboratory for Optoelectronics and School of Physics, Huazhong University of Science and Technology, Wuhan 430074, China

**Shaolin Ke** – Hubei Key Laboratory of Optical Information and Pattern Recognition, Wuhan Institute of Technology, Wuhan 430025, China

**Dong Zhao** – Department of Optics and Optical Engineering, University of Science and Technology of China, Hefei, Anhui 230026, China

**Jianghua Ye** – Wuhan National Laboratory for Optoelectronics and School of Physics, Huazhong University of Science and Technology, Wuhan 430074, China

**Yanan Wang** – Wuhan National Laboratory for Optoelectronics and School of Physics, Huazhong University of Science and Technology, Wuhan 430074, China

**Kun Huang** – Department of Optics and Optical Engineering, University of Science and Technology of China, Hefei, Anhui 230026, China; [orcid.org/0000-0002-9391-149X](https://orcid.org/0000-0002-9391-149X)

**Peixiang Lu** – Wuhan National Laboratory for Optoelectronics and School of Physics, Huazhong University of Science and Technology, Wuhan 430074, China; Hubei Key Laboratory of Optical Information and Pattern Recognition, Wuhan Institute of Technology, Wuhan 430025, China

Complete contact information is available at:

<https://pubs.acs.org/10.1021/acs.nanolett.3c05095>

### Author Contributions

<sup>†</sup>S.C., S.K., and D.Z. contributed equally to this work.

### Notes

The authors declare no competing financial interest.

## ■ ACKNOWLEDGMENTS

This work was supported by the National Natural Science Foundation of China (No. 62375097, No. 12374305, No. 12021004), the Natural Science Foundation of Hubei Province (No. 2023AFB822), and Hubei Key Laboratory of Optical Information and Pattern Recognition, Wuhan Institute of Technology (No. 202202).

## ■ REFERENCES

- (1) Yuan, L.; Shi, Y.; Fan, S. Photonic gauge potential in a system with a synthetic frequency dimension. *Opt. Lett.* **2016**, *41* (4), 741–744.
- (2) Fang, K.; Yu, Z.; Fan, S. Photonic Aharonov-Bohm effect based on dynamic modulation. *Phys. Rev. Lett.* **2012**, *108* (15), 153901.
- (3) Lin, Q.; Fan, S. Light Guiding by Effective Gauge Field for Photons. *Phys. Rev. X* **2014**, *4* (3), 031031.
- (4) Lu, C.; Liu, Z.; Wu, Y.; Xiao, Z.; Yu, D.; Zhang, H.; Wang, C.; Hu, X.; Liu, Y. C.; Liu, X.; Zhang, X. Nanophotonic Polarization

- Routers Based on an Intelligent Algorithm. *Adv. Optical Mater.* **2020**, *8* (10), 1902018.
- (5) Qin, C.; Zhou, F.; Peng, Y.; Sounas, D.; Zhu, X.; Wang, B.; Dong, J.; Zhang, X.; Alu, A.; Lu, P. Spectrum Control through Discrete Frequency Diffraction in the Presence of Photonic Gauge Potentials. *Phys. Rev. Lett.* **2018**, *120* (13), 133901.
- (6) Li, W.; Yang, N.; Chen, H.; Wang, B.; Qin, C.; Han, T.; Zhang, Y.; Liu, W.; Zhang, C.; Zhang, X.; Lu, P. Broadband frequency control of light using synthetic frequency lattices formed by four-wave-mixing Bragg scatterings. *Phys. Rev. A* **2021**, *103* (3), 033514.
- (7) Lumer, Y.; Bandres, M. A.; Heinrich, M.; Maczewsky, L. J.; Herzig-Sheinfux, H.; Szameit, A.; Segev, M. Light guiding by artificial gauge fields. *Nat. Photonics* **2019**, *13* (5), 339–345.
- (8) Plotnik, Y.; Bandres, M. A.; Stützer, S.; Lumer, Y.; Rechtsman, M. C.; Szameit, A.; Segev, M. Analogue of Rashba pseudo-spin-orbit coupling in photonic lattices by gauge field engineering. *Phys. Rev. B* **2016**, *94* (2), 020301.
- (9) Li, E.; Eggleton, B. J.; Fang, K.; Fan, S. Photonic Aharonov-Bohm effect in photon-phonon interactions. *Nat. Commun.* **2014**, *5*, 3225.
- (10) Fang, K.; Fan, S. Controlling the flow of light using the inhomogeneous effective gauge field that emerges from dynamic modulation. *Phys. Rev. Lett.* **2013**, *111* (20), 203901.
- (11) Zhao, H.; Qiao, X.; Wu, T.; Midya, B.; Longhi, S.; Feng, L. Non-Hermitian topological light steering. *Science* **2019**, *365* (6458), 1163–1166.
- (12) Guo, Z.; Wang, Y.; Ke, S.; Su, X.; Ren, J.; Chen, H. 1D Photonic Topological Insulators Composed of Split Ring Resonators: A Mini Review. *Adv. Physics Res.* **2023**, 2300125.
- (13) Yu, D.; Yuan, L.; Chen, X. Isolated Photonic Flatband with the Effective Magnetic Flux in a Synthetic Space Including the Frequency Dimension. *Laser Photonics Rev.* **2020**, *14* (11), 2000041.
- (14) Vidal, J.; Mosseri, R.; Douçot, B. Aharonov-Bohm Cages in Two-Dimensional Structures. *Phys. Rev. Lett.* **1998**, *81* (26), 5888.
- (15) Longhi, S. Aharonov-Bohm photonic cages in waveguide and coupled resonator lattices by synthetic magnetic fields. *Opt. Lett.* **2014**, *39* (20), 5892–5895.
- (16) Di Liberto, M.; Mukherjee, S.; Goldman, N. Nonlinear dynamics of Aharonov-Bohm cages. *Phys. Rev. A* **2019**, *100* (4), 043829.
- (17) Vidal, J.; Butaud, P.; Douçot, B.; Mosseri, R. Disorder and interactions in Aharonov-Bohm cages. *Phys. Rev. B* **2001**, *64* (15), 155306.
- (18) Jorg, C.; Queralto, G.; Kremer, M.; Pelegri, G.; Schulz, J.; Szameit, A.; von Freymann, G.; Mompert, J.; Ahufinger, V. Artificial gauge field switching using orbital angular momentum modes in optical waveguides. *Light. Sci. Appl.* **2020**, *9*, 150.
- (19) Ke, S.; Zhao, D.; Fu, J.; Liao, Q.; Wang, B.; Lu, P. Topological Edge Modes in Non-Hermitian Photonic Aharonov-Bohm Cages. *IEEE J. Sel. Top. Quantum Electron.* **2020**, *26* (6), 1–8.
- (20) Zhang, S. M.; Jin, L. Compact localized states and localization dynamics in the dice lattice. *Phys. Rev. B* **2020**, *102* (5), 054301.
- (21) Tang, L.; Song, D.; Xia, S.; Xia, S.; Ma, J.; Yan, W.; Hu, Y.; Xu, J.; Leykam, D.; Chen, Z. Photonic flat-band lattices and unconventional light localization. *Nanophotonics* **2020**, *9* (5), 1161–1176.
- (22) Mukherjee, S.; Spracklen, A.; Choudhury, D.; Goldman, N.; Ohberg, P.; Andersson, E.; Thomson, R. R. Observation of a Localized Flat-Band State in a Photonic Lieb Lattice. *Phys. Rev. Lett.* **2015**, *114* (24), 245504.
- (23) Mukherjee, S.; Thomson, R. R. Observation of localized flat-band modes in a quasi-one-dimensional photonic rhombic lattice. *Opt. Lett.* **2015**, *40* (23), 5443–5446.
- (24) Mukherjee, S.; Di Liberto, M.; Ohberg, P.; Thomson, R. R.; Goldman, N. Experimental Observation of Aharonov-Bohm Cages in Photonic Lattices. *Phys. Rev. Lett.* **2018**, *121* (7), 075502.
- (25) Caceres-Aravena, G.; Guzman-Silva, D.; Salinas, I.; Vicencio, R. A. Controlled Transport Based on Multiorbital Aharonov-Bohm Photonic Caging. *Phys. Rev. Lett.* **2022**, *128* (25), 256602.
- (26) Kremer, M.; Petrides, I.; Meyer, E.; Heinrich, M.; Zilberberg, O.; Szameit, A. A square-root topological insulator with non-quantized indices realized with photonic Aharonov-Bohm cages. *Nat. Commun.* **2020**, *11* (1), 907.
- (27) Wang, H.; Zhang, W.; Sun, H.; Zhang, X. Observation of inverse Anderson transitions in Aharonov-Bohm topoelectrical circuits. *Phys. Rev. B* **2022**, *106* (10), 104203.
- (28) Pelegri, G.; Marques, A. M.; Dias, R. G.; Daley, A. J.; Mompert, J.; Ahufinger, V. Topological edge states and Aharonov-Bohm caging with ultracold atoms carrying orbital angular momentum. *Phys. Rev. A* **2019**, *99* (2), 023613.
- (29) Li, H.; Dong, Z.; Longhi, S.; Liang, Q.; Xie, D.; Yan, B. Aharonov-Bohm Caging and Inverse Anderson Transition in Ultracold Atoms. *Phys. Rev. Lett.* **2022**, *129* (22), 220403.
- (30) Hafezi, M.; Demler, E. A.; Lukin, M. D.; Taylor, J. M. Robust optical delay lines with topological protection. *Nat. Phys.* **2011**, *7* (11), 907–912.
- (31) Harari, G.; Bandres, M. A.; Lumer, Y.; Rechtsman, M. C.; Chong, Y. D.; Khajavikhan, M.; Christodoulides, D. N.; Segev, M. Topological insulator laser: Experiments. *Science* **2018**, *359*, No. eaar4005.
- (32) Lin, Z.; Ding, L.; Ke, S.; Li, X. Steering non-Hermitian skin modes by synthetic gauge fields in optical ring resonators. *Opt. Lett.* **2021**, *46* (15), 3512–3515.
- (33) Gu, Z.; Gao, H.; Xue, H.; Li, J.; Su, Z.; Zhu, J. Transient non-Hermitian skin effect. *Nat. Commun.* **2022**, *13* (1), 7668.
- (34) Hafezi, M.; Mittal, S.; Fan, J.; Migdall, A.; Taylor, J. M. Imaging topological edge states in silicon photonics. *Nat. Photonics* **2013**, *7* (12), 1001–1005.
- (35) Longhi, S.; Gatti, D.; Della Valle, G. Robust light transport in non-Hermitian photonic lattices. *Sci. Rep.* **2015**, *5*, 13376.
- (36) Song, Y.; Liu, W.; Zheng, L.; Zhang, Y.; Wang, B.; Lu, P. Two-dimensional non-Hermitian Skin Effect in a Synthetic Photonic Lattice. *Phys. Rev. Applied* **2020**, *14* (6), 064076.
- (37) Harari, G.; Bandres, M. A.; Lumer, Y.; Rechtsman, M. C.; Chong, Y. D.; Khajavikhan, M.; Christodoulides, D. N.; Segev, M. Topological insulator laser: Theory. *Science* **2018**, *359*, No. eaar4003.
- (38) Liu, W.; Zhang, Y.; Deng, Z.; Ye, J.; Wang, K.; Wang, B.; Gao, D.; Lu, P. On-Chip Chiral Mode Switching by Encircling an Exceptional Point in an Anti-Parity-Time Symmetric System. *Laser Photonics Rev.* **2022**, *16* (12), 2100675.
- (39) Kempkes, S. N.; Capiod, P.; Ismaili, S.; Mulkens, J.; Eek, L.; Swart, I.; Morais Smith, C. Compact localized boundary states in a quasi-1D electronic diamond-necklace chain. *Quantum Front* **2023**, *2* (1), 1.
- (40) Liu, L.; Li, T.; Zhang, Q.; Xiao, M.; Qiu, C. Universal Mirror-Stacking Approach for Constructing Topological Bound States in the Continuum. *Phys. Rev. Lett.* **2023**, *130* (10), 106301.